

Chapter 9

Energy Harvesting from Fluids Using Ionic Polymer Metal Composites

Maurizio Porfiri and Sean D. Peterson

Abstract In this chapter, we discuss energy harvesting from steady, oscillatory, and unsteady water flows using ionic polymer metal composites (IPMCs). After a brief description of this new class of active materials and their ability to transduce strain energy into electrical form, we present three case studies spanning this range of flow environments. First, we examine energy harvesting from a heavy flapping flag hosting IPMCs in a steady flow water channel; second, we consider base excitation of a cantilevered IPMC to simulate the effect of an oscillatory flow; and finally, we investigate the impact of a vortex ring with an IPMC. Analytical insight on the mechanics of the coupled fluid–structure problem is used to interpret experimental results and provide design guidelines for energy harvesters based on active compliant materials in fluids.

9.1 Introduction

Recent progress in lightweight smart materials has opened the door to scientific and technological advancements in the area of energy harvesting [30]. Energy extracted from the surroundings can be potentially used to power low consumption electronic devices [20, 35, 39, 40, 47, 66, 82]. The main advantages over traditional batteries of powering devices via energy harvesting are extended device lifetime, limited

M. Porfiri (✉)

Department of Mechanical and Aerospace Engineering, Polytechnic Institute of New York University, 6 Metrotech Center, Brooklyn, NY 11201 USA

e-mail: mporfiri@poly.edu

S.D. Peterson

Department of Mechanical and Mechatronics Engineering, University of Waterloo, 200 University Avenue West, Waterloo, ON N2L 3G1 Canada

e-mail: peterston@mme.uwaterloo.ca

maintenance, and reduced onboard weight. Comprehensive overviews of energy harvesting methods and implementations can be found in [49, 51, 68, 87].

Mechanical vibration has received particular attention as a simple and viable source for energy harvesting using active materials. In this context, piezoelectrics have seen considerable research efforts in the conversion of mechanical energy into electrical energy via deformation (see the reviews in [7, 75]). Energy harvesting from the base excitation of cantilevered piezoelectric beams is analytically studied and experimentally validated in [28, 29]. The feasibility of enhancing the energy harvesting capabilities of piezoelectrics through shunting and nonlinear circuit elements is presented in [38] and strategies for optimization of design parameters are discussed in [43, 67]. Methods for expanding the frequency range and storing electric energy from piezoelectric harvesters are discussed in [46, 76, 77].

The momentum carried by research on piezoelectric energy harvesting of mechanical vibration has sparked into emerging interest for exploring alternative uses of piezoelectrics for energy scavenging. Specifically, a few implementations of piezoelectrics in fluidic energy harvesting, wherein the fluid is used as a source of energy instead of a passive damper, have been recently presented. Drawing inspiration from traditional windmills, the design of a small scale piezoelectric-based windmill is presented in [53]. Energy harvesting from a piezoelectric strip placed in the wake of a cylinder in the direction of the cross flow is studied in [6, 81]. Therein, the strip is subject to the time-varying pressure loading caused by the Kármán vortex street shed from the cylinder. A similar configuration placed in a turbulent boundary layer is considered in [2]. Structural instabilities induced by the fluid coupling are explored in [21, 31, 78]. Specifically, fluttering structures for energy harvesting are described in [21, 31] and flow-induced self-oscillations of structures hosting piezoelectrics are considered in [78].

While piezoelectrics offer several advantages over other active materials in terms of energy harvesting, including a good energy conversion rate and reliable performance, their implementation in harvesting fluid energy as miniature devices can be limited by their stiffness, brittleness, and challenges associated with working in wet environments. Ionic polymer metal composites (IPMCs), sometimes referred to as ionic polymer transducers, are a novel class of electro-active polymers that are currently receiving considerable attention for their propitious attributes for both sensing and actuation. An IPMC is a porous ionic polymer saturated with an electrolytic solution and plated by noble metal electrodes (see for example [70]). Mechanical deformation yields a voltage difference across the electrodes, and, similarly, a voltage difference across the electrodes produces structural deformations. The electrolytic solution comprises a mobile counterion species and an uncharged solvent. Sensing and actuation are the result of interactions between the mobile ions and the solvent, and between the solvent and the backbone polymer [56]. A comprehensive review of modeling, fabrication, and applications of IPMCs up to the early part of this decade can be found in [44, 71–73]. Recent modeling efforts include black-box linear and nonlinear models [16–18, 37] and physics-based models that employ multiphase mixture theory and Poisson–Nernst–Planck equations (see, e.g., [22, 23, 26, 41, 54, 55, 57, 61, 62, 84–86]). Advanced fabrication

techniques are presented in [3, 4]. Recent applications span underwater propulsion systems [1, 9, 42, 50, 60, 88], force and displacement sensors [15, 19, 34, 70], and grippers and manipulation systems [27, 33, 45].

Despite their considerable use as sensors and actuators, there are few demonstrations of IPMC-based energy harvesting. Specifically, energy harvesting from mechanical vibrations in air is demonstrated in [20, 35, 82]. In [82], IPMCs consisting of two different electrode materials are tested and compared under cyclic bending, tension, and shear. Analytical insight into base excitation of IPMCs in air along with experimental results is reported in [20]. Longitudinal vibrations in air are modeled, tested, and compared with results from piezoelectrics in [35].

In this book chapter, we report the implementation of IPMCs as fluid energy harvesters in three different conditions exemplifying steady, oscillatory, and unsteady flows. Specifically, we summarize the integration of IPMCs in flapping flags underwater presented in [36], the base excitation of IPMC strips in water studied in [13], and the interaction between IPMCs and coherent fluid structures described in [58, 59].

9.2 IPMC Energy Conversion

As a first approximation, the IPMC sensing behavior can be described by using a lumped circuit model comprising a linear impedance in series with a voltage source that depends on the IPMC mechanical deformation. This model is derived starting from a Poisson–Nernst–Planck model of the dynamics of the counterion concentration and the electric potential within the ionomeric membrane following [13]. In this model, IPMC deformation acts as a forcing term in Poisson’s equation, wherein the free charge density is described by the concentration of the mobile counterions and of the fixed charges, which varies as the IPMC deforms. The modeling approach presented therein discards convective terms in the governing equations and surface roughness of IPMC electrodes [10, 63] and focuses on small deformations producing voltage levels smaller than the thermal voltage.

Within this lumped circuit model, the linear impedance is found to be the series connection of a resistor \mathcal{R} and a capacitor \mathcal{C} . The resistor accounts for the ion diffusion in the ionomeric membrane and it can practically be used to incorporate the resistivity of the plating electrodes. The capacitor embodies bulk and double layer effects [14] in the vicinity of the IPMC electrodes and is highly correlated to the electrode surface roughness [10, 63]. The voltage source describes IPMC sensing and is proportional to the rate of change in time t of the relative rotation $\vartheta(t)$ between the IPMC ends through the constant \mathcal{B}/\mathcal{C} , that is,

$$V_{\text{oc}}(t) = \frac{\mathcal{B}}{\mathcal{C}} \frac{d\vartheta(t)}{dt} \quad (9.1)$$

Here, \mathcal{B} represents an electromechanical gain, and subscript OC is used to emphasize that this voltage is the IPMC output when its terminals are left open circuited. For convenience, we refer to the rate of change of $\vartheta(t)$ as $\Omega(t)$. We further note that Eq. (9.1) implies that the overall voltage drop across the IPMC depends only on the differences between the rotations at its ends that is a measure of the average IPMC curvature. This is due to the fact that the original physics-based model assumes that the electrodes are perfect conductors.

By considering oscillations at the radian frequency ω and using a superimposed hat to identify phasors, the voltage $\hat{V}(\omega)$ across the IPMC is

$$\hat{V}(\omega) = \frac{\hat{I}(\omega)}{Y(\omega)} - \frac{\mathcal{B}}{\mathcal{C}} \hat{\Omega}(\omega) \quad (9.2)$$

where the IPMC electrical admittance $Y(\omega)$ equals $i\omega\mathcal{C}/(1 + i\omega\mathcal{R}\mathcal{C})$ and $I(t)$ is the current through the IPMC. Thus, the IPMC response is described by using only the parameters \mathcal{C} , \mathcal{R} , and \mathcal{B} that are experimentally identified from a discharge experiment along with an open circuit, or short circuit, measurement by following the procedure described in [13]. We further comment that if convective terms are taken into consideration, the expression for $V_{OC}(t)$ is modified to favor a dependence on the relative rotation as compared to its time derivative [11]. Practically, given the experimental identification of the electromechanical gain, the noise in experimental data and the relatively narrow range of vibrations typically considered for energy harvesting, both the approaches may be suitable.

When the IPMC electrodes are connected to an external resistive load R_l , its average power output is

$$\hat{P}(\omega) = \frac{1}{2} \frac{|\hat{V}(\omega)|^2}{R_l} = \frac{1}{2} \frac{\omega^2 \mathcal{B}^2}{(\mathcal{R} + R_l)^2 \omega^2 \mathcal{C}^2 + 1} R_l |\hat{\Omega}(\omega)|^2 \quad (9.3)$$

The resistance that maximizes the power transfer is found by setting $\partial \hat{P}(\omega)/\partial R_l = 0$, that is,

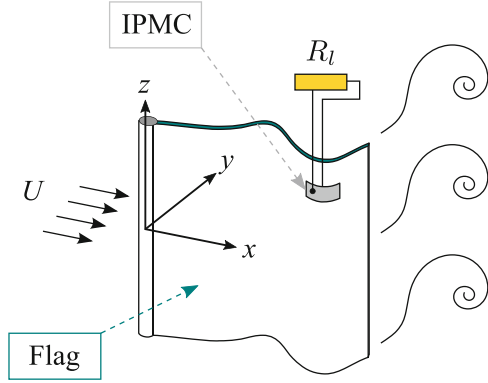
$$R_l^{\text{opt}}(\omega) = \frac{1}{\omega\mathcal{C}} \sqrt{1 + \omega^2 \mathcal{T}^2} \quad (9.4)$$

where the time constant of the equivalent IPMC circuit is defined as $\mathcal{T} = \mathcal{R}\mathcal{C}$.

9.3 Energy Harvesting from Flapping Flags

Here, we report on an energy harvester based on a heavy and flexible flag flapping in a uniform water flow hosting an IPMC, as designed in [36] and shown in Fig. 9.1. The physics of the fluid–structure interaction and the resulting instability of the fluttering flag can be elucidated by considering the propagation of waves in a fluid-loaded elastic plate [25]. We consider the two-dimensional incompressible inviscid

Fig. 9.1 Schematic of the flexible heavy flag flapping in a uniform water stream of velocity U , comprising the host structure and IPMC strip (Reprinted with permission from [36]. Copyright 2011, American Institute of Physics)



flow with free stream speed U and density ρ over a thin elastic plate of infinite extension along the x direction. Following [74], we neglect the near field solutions and the effect of the wake on the instability boundary [5, 80] to derive a simple closed-form expression for the flutter boundary.

We model the structure as a homogenous Kirchhoff–Love plate of length L_{flag} , width w_{flag} , bending stiffness per unit width B_{flag} , and mass per unit length m_{flag} undergoing cylindrical bending [48]. The plate is subject to a pretension T due to the fluid boundary layer and to the pressure of the surrounding fluid. The plate is coupled to the fluid problem by following [5], where the flag boundary is modeled as a bound vortex and the relative fluid velocity at the flag is set to zero. From dimensional analysis, we find that the fundamental nondimensional groups are

$$R_1 = \frac{m_{\text{flag}}}{\rho L_{\text{flag}} w_{\text{flag}}}, \quad R_2 = \frac{B_{\text{flag}}}{\rho U^2 L_{\text{flag}}^3}, \quad \beta = \frac{T L_{\text{flag}}^2}{B_{\text{flag}}} \quad (9.5)$$

These parameters describe the mass ratio between the flag and the surrounding fluid, the ratio between elastic and fluid forces, and the stiffening effect of the tension T with respect to the flag’s inherent bending stiffness, respectively.

By analyzing the linear stability of a the fundamental propagating wave, that is, a vibration with wavelength equal to L_{flag} , we obtain a closed-form expression for the onset of flutter as a function of the three nondimensional parameters. The stability is represented in Fig. 9.2 with the stable region in the upper left side of the plot. The space (R_1, R_2, β) allows visual identification of the effect of flag mass, velocity, and tension on the stability boundary. In particular, increasing values of the tension tend to stabilize the system, while increasing values of the flag mass have the opposite effect.

The host flag is constructed following [74]: a Mylar sheet of thickness $26 \mu\text{m}$ constitutes the flexible membrane, and copper strips of dimension $102 \times 6.7 \times 0.4 \text{ mm}^3$ are glued every 4.4 mm of bare Mylar on both sides to increase the mass per unit length of the flag. The IPMC sample is integrated in the structure by

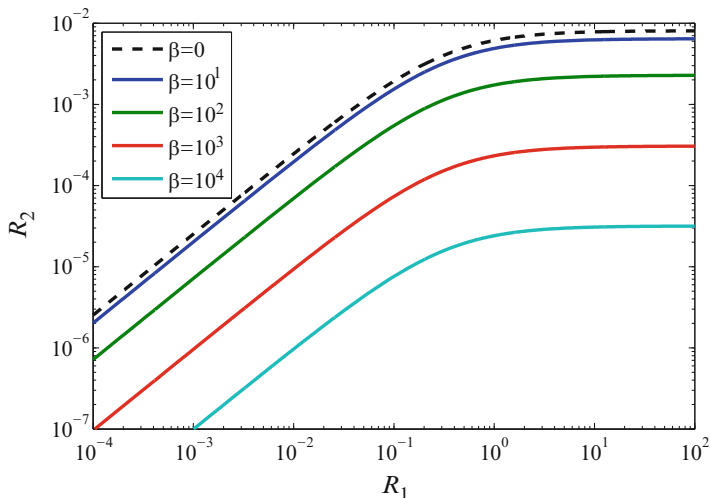


Fig. 9.2 Linear stability plot as the tension to bending stiffness ratio β is varied. The region above the boundary identifies stable oscillations of the system. In the region below the boundary the system is unstable. The *dashed line* represents the case $T = 0$ (Reprinted with permission from [36]. Copyright 2011, American Institute of Physics)

clamping it within the copper strips. The mechanical parameters of the heavy flag, that is, the mass per unit length and the bending stiffness, are estimated from its periodic structure and the physical parameters of the constituent materials yielding $B_{\text{flag}} = 2 \times 10^{-5} \text{ N m}$ and $m_{\text{flag}} = 0.45 \text{ kg/m}$. The tension in the flag is estimated using the Blasius boundary layer solution for an infinite plate theory following [24]. From Eq. (9.5) and Fig. 9.2, we estimate that the critical flow speed of flutter instability is $U_c = 0.23 \text{ m/s}$, as what occurs beyond this speed would likely be bounded nonlinear limit-cycle oscillations.

The IPMC harvester is fabricated in-house from commercial Nafion membrane foils N117 produced by DuPont de Nemours by following the procedure developed by Oguro from Osaka National Research Institute, AIST, Japan (see also [10]). The nominal dimensions of the sample are $33 \times 11 \times 0.2 \text{ mm}^3$ and the resistance \mathcal{R} and capacitance \mathcal{C} are 390Ω and $4 \mu\text{F}$, respectively.

The device is immersed in the test section of a water tunnel of nominal dimensions $2500 \times 150 \times 150 \text{ mm}^3$ filled with tap water and the onset and development of the flutter instability is studied for increasing velocities. The water speed is measured with laser Doppler velocimetry, the post-flutter vibrations are tracked by means of image analysis and the time trace of the voltage across the load R_l is recorded with a data acquisition (DAQ) board.

A qualitative analysis of the flow before and after the onset of flapping can be garnered through flow visualization as illustrated in Fig. 9.3. In Fig. 9.3a, representing a flow speed of $U = 0.4 \text{ m/s}$, the vortex sheet aligns itself to the flow direction. In Fig. 9.3b,c, the periodic release of vorticity having alternating signs is

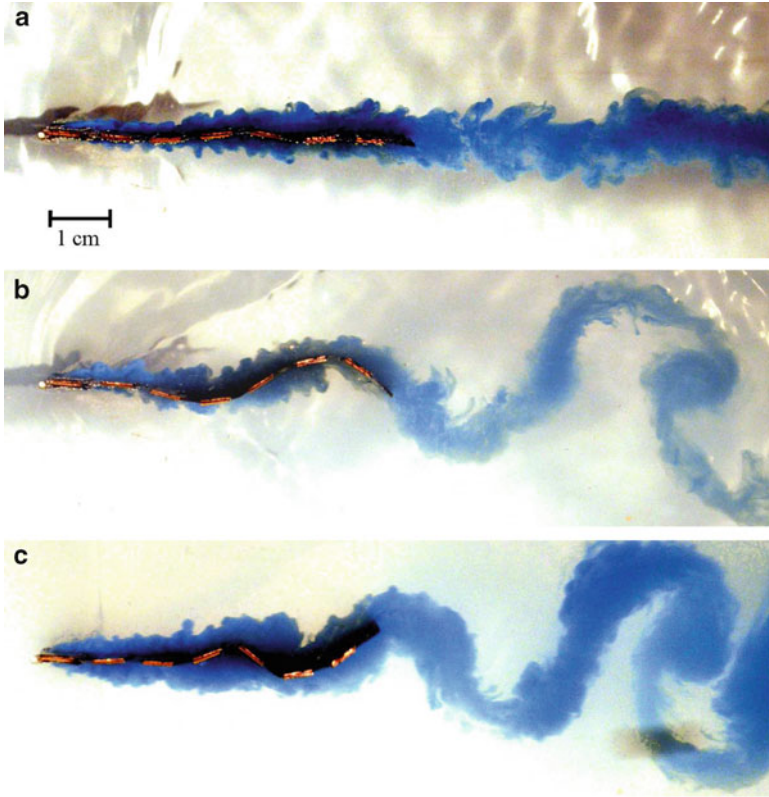


Fig. 9.3 Flow visualization of the vortex sheet originating on the boundary of the flag and released in the wake. Images are captured (a) before and (b)–(c) after the onset of flutter, for free stream speed values of 0.4, 0.6, and 0.8 m/s, respectively (Reprinted with permission from [36]. Copyright 2011, American Institute of Physics)

made evident by the dye lines. The free stream velocities are 0.4, 0.6 and 0.8 m/s, respectively. The shedding frequency increases with the background flow speed as can be deduced from the different numbers of folds in the wake sheets.

From the direct measurement of the IPMC voltage output for varying R_l , in Fig. 9.4 we present an estimate of the scavenged power. The maximum power conversion is obtained when the load resistance is $R_l = 10 \text{ k}\Omega$, in line with the prediction of Eq. (9.4) for the considered range of vibration frequencies on the order of a few Hertz. The harvested power in the optimal conditions lies in the range 10^{-12} – 10^{-10} W. This estimate is conservative since it neglects the energy content of higher harmonics that can be exploited in real applications. The power harnessed from the flow can be increased by enlarging the portion of flag surface area covered with IPMC strips. In this prototype, the IPMC strip covers approximately 2% of the area of the active flag and contributes to approximately 0.5% of its weight.

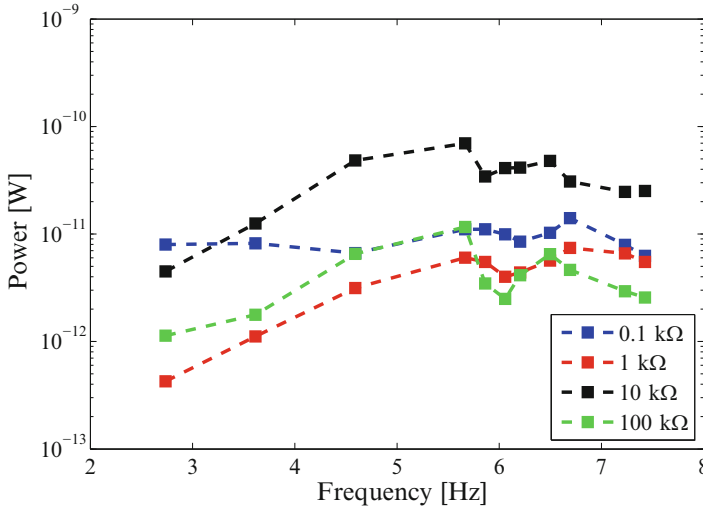


Fig. 9.4 Harvested power as a function of flapping frequency and load resistance. The estimate is performed by including harmonic components within ± 0.3 Hz from the flapping frequency in the computation of the voltage amplitude (Reprinted with permission from [36]. Copyright 2011, American Institute of Physics)

9.4 Energy Harvesting from an Oscillating Fluid

Here, we consider energy harvesting from the base excitation of a cantilevered IPMC to explore the mechanics of energy scavenging from oscillatory flows. Unlike the problem considered above, in this case the IPMC is the sole structural element. Specifically, we consider a cantilevered IPMC rectangular strip vibrating in a fluid in response to harmonic base excitation of its clamped end.

The energy available for harvesting can be estimated from the analysis of a simplified model of the coupled fluid–structure problem, wherein the IPMC is modeled as a Kirchhoff–Love plate undergoing cylindrical bending and the effect of the encompassing fluid is lumped into a hydrodynamic function [8, 12, 32, 69, 83]. Such function describes both added mass and viscous damping from the surrounding fluid and can be derived by solving an auxiliary two-dimensional problem where a rigid lamina, identifying a generic beam cross section, periodically oscillates in the fluid. For small vibrations compared to the IPMC width, convective terms in the Navier–Stokes equations can be discarded in favor of an unsteady Stokes flow, which yields a hydrodynamic function that depends exclusively on the oscillatory Reynolds number [69, 83]. If oscillations become more severe, vorticity shedding and advection in the flow becomes dominant and the dependence of the hydrodynamic function on the Keulegan–Carpenter number, related to the ratio between the oscillation amplitude and the width, should be taken into consideration to elucidate nonlinear damping [8, 12, 32].

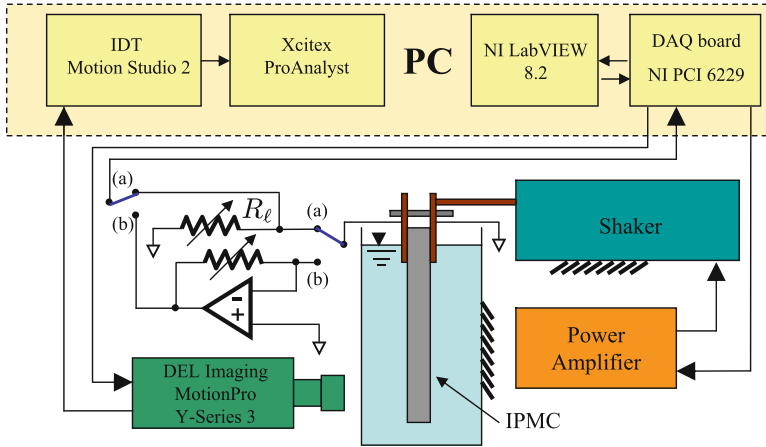


Fig. 9.5 Schematics of the experimental setup from [13]. The switch positions (a) and (b) allow for voltage, current, and power measurements in open circuit, short circuit, and loaded conditions

The IPMC sample used in this study, purchased from Environmental Robots, Inc., has nominal dimensions of $30 \times 5.8 \times 0.2 \text{ mm}^3$. The mass per unit length of the sample is $3.48 \times 10^{-3} \text{ kg/m}$. The undamped in-vacuum fundamental natural frequency is 12.5 Hz and the in-vacuum loss factor is 0.14, yielding an IPMC bending stiffness per unit width of $B = 1.2 \times 10^{-4} \text{ N m}$. The IPMC sample is tested in a 2 l pool of deionized water. The sample is arranged in a cantilever configuration with a free vibration length of $L = 25 \text{ mm}$ and the clamped end rigidly attached to a shaker to produce the base excitation. The shaker is driven with a sinusoidal voltage signal with the actuation frequency varied from 2 to 50 Hz. The clamp is electrically connected to a DAQ board to record the voltage output of the IPMC (see Fig. 9.5). The actual motion of the clamped edge of the IPMC is constantly monitored by using a laser displacement sensor. The IPMC lateral displacement is recorded through a high-speed camera and then analyzed using a commercial software.

Figure 9.6 displays experimental data on the IPMC frequency response defined by taking the base excitation as the input and the tip deflection, that is, the difference between the tip displacement and the rigid body motion, as the output. The discrepancy between the theoretical predictions from the linear theory highlights the importance of vorticity shedding in the mechanics of fluid–structure interactions. On the other hand, the model in [8] is able to reasonably capture the magnitude and the phase of the transfer function for low to moderately high frequencies. Discrepancies in the high-frequency region of the phase diagram may be attributed to noise amplification due to the indirect nature of the relative tip displacement measurements. We note that in the considered broad frequency interval, the magnitude of the transfer function varies in a rather limited range. This hints that energy harvesting may be possible in a variety of loading conditions that are typically present in underwater systems, such as wave slamming [64] and structural vibrations [52].

Fig. 9.6 Frequency response of the IPMC tip deflection. *Red markers* are experimental data, *solid line* is the prediction using unsteady Stokes flow from [69, 83], and *black markers* are predictions from the nonlinear hydrodynamic model in [8]

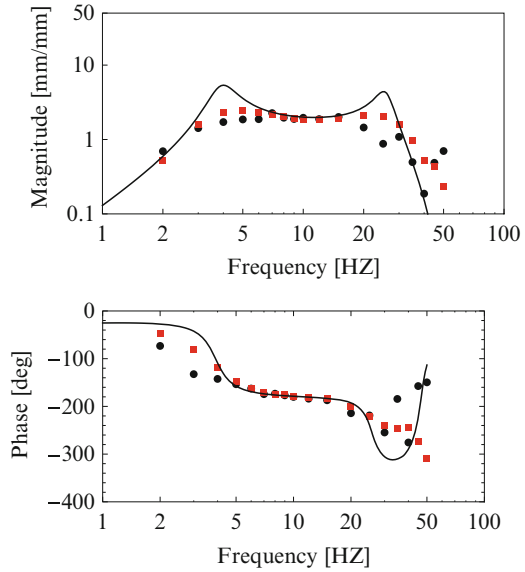
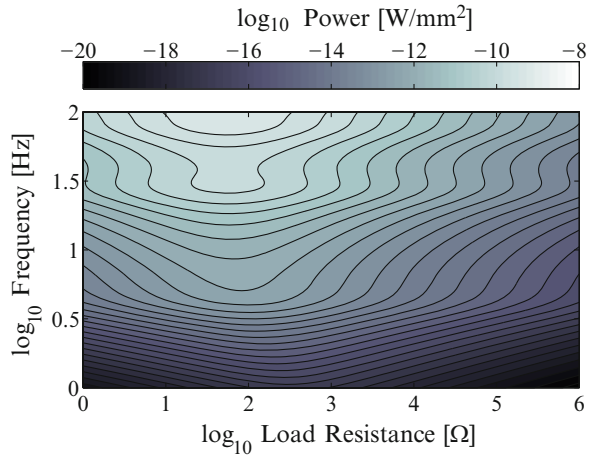


Fig. 9.7 Theoretical harvested power from IPMC underwater vibration from [13]



Two different experiments are performed to establish the feasibility of the vibrating IPMC as an energy harvester. In the first experiment, the IPMC is shunted with a resistor R_l , while in the second experiment, the short circuit current through the IPMC is measured. The electric parameters of the IPMC are $\mathcal{R} = 55.2 \Omega$ and $\mathcal{C} = 0.51 \text{ mF}$. The electromechanical coupling is $\mathcal{B} = 2.286 \times 10^{-9} \text{ A s}^2/\text{rad}$, which is comparable to the one for the flapping flag described above $1.85 \times 10^{-10} \text{ A s}^2/\text{rad}$.

Further, we determine the power harvested from the IPMC underwater vibration under loaded conditions by using Eq. (9.3) with the parameters discussed above. The influence of the vibration frequency and the electrical load on the harvested power is shown in Fig. 9.7, which is obtained by using the frequency response in Fig. 9.6.

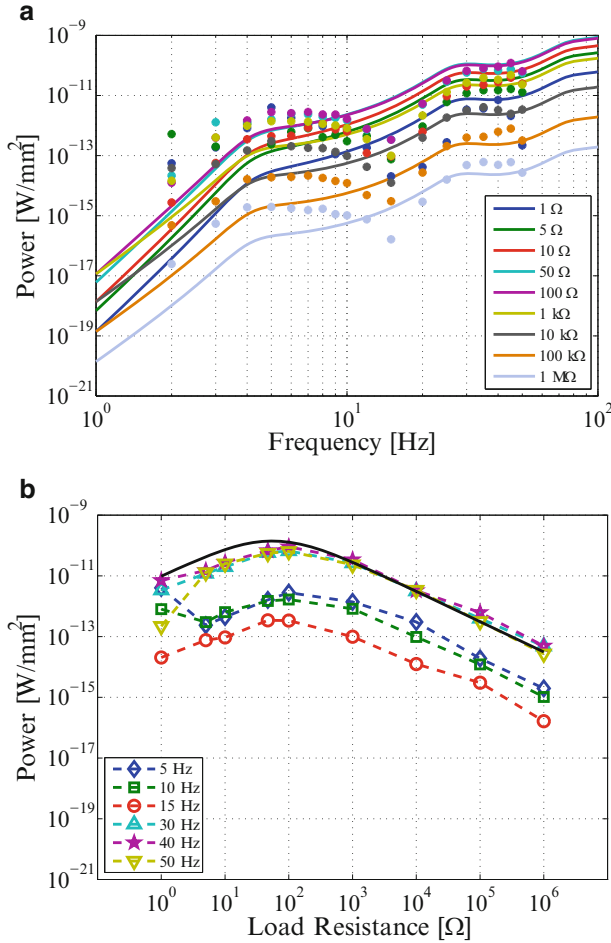


Fig. 9.8 (a) Comparison between the theoretical and experimental (points) power harvesting capability of the vibrating IPMC, from [13]. (b) Experimental data on power harvesting as a function of the shunting resistance. The *solid line* represents theoretical predictions

Note that nonlinear damping due to vorticity shedding is here approximated as a surplus of structural damping to simplify the parametric analysis. Figure 9.7 presents a contour map identifying optimal regions of operation for the harvesting device. The harvested power varies in the range 10⁻²⁰–10⁻⁸ W/mm² and significantly increases with increasing actuation frequency. In particular, the maxima of the harvested power occur when the actuation frequency matches the underwater resonance frequencies of the vibrating IPMC. That is, a flow oscillating at the underwater resonance frequency of the harvester will maximize the energy scavenged.

Experimental results are compared with theoretical predictions of power harvested versus input frequency in Fig. 9.8a. The curves in Fig. 9.8a show the

trends of the harvested power with respect to the base excitation frequency and are parameterized with respect to the load resistance R_l . Figure 9.8b shows the dependence of the output power on the load resistance along with the existence of a maximum in correspondence to a shunting resistance in the range 10–100 Ω . The harvested power is computed using Eq. (9.3). We note that power harvested is expected to depend nonlinearly on the oscillation amplitude due to nonlinear hydrodynamic damping [8].

9.5 Energy Harvesting from Coherent Fluid Structures

Here, we consider energy harvesting from coherent fluid structures, summarizing results from [58, 59]. Specifically, we study the mechanics of energy transfer from a self-propagating vortex ring in an otherwise placid fluid to an IPMC via impact. The IPMC harvester is fabricated in-house from commercial Nafion membrane foils N117 as per the flapping flag experiment. It has a total length of 36.6 mm, a nominal thickness of 200 μm , a width of $w = 14.3$ mm, its mass per unit length is $m = 5.63$ g/m, and its bending stiffness per unit width is $B = 2.83 \times 10^{-4}$ N m. The IPMC is fixed at one end by a custom clamping device with copper electrodes adhered to each arm of the clamp and immersed in a tank of dimensions $415 \times 236 \times 215$ mm³ that is filled with tap water (see Fig. 9.10). The free vibration length is $L = 21.0$ mm and corresponds to a vibrating mass of 118 mg. In this configuration, the IPMC electrical capacitance is $\mathcal{C} = 37.8$ μF .

The vortex ring is generated by a piston submerged in water plunged through a cylinder with internal diameter of 19.1 mm. Experiments are conducted at room temperature and the water density is taken at its reference value of $\rho = 1,000$ kg/m³. The stroke length of the piston is 75.0 mm, and the cylinder has a flat, sharp-edged exit plane. The piston is placed 165 mm below the free surface of the tank and 115 mm from the IPMC. It is situated such that the center of the vortex ring is approximately aligned with the tip of the IPMC and the direction of propagation of the ring is orthogonal to its rest position. Figure 9.9 illustrates a flow visualization experiment in which a high-speed video camera is used to record the fluid motion and the IPMC vibration. As the piston plunges into the cylinder, water is expelled and the resulting shear layer rolls up into a vortex ring. Once the plunger stops, vorticity is no longer formed and the vortex ring propagates towards the IPMC at a nearly constant speed due to self-induction. As the vortex ring approaches the IPMC, the IPMC slowly bends away from the vortex ring, and as it reaches the rest position of the IPMC, the energy transfer dramatically increases resulting in rapid and severe structural deflections.

We use time-resolved particle image velocimetry (PIV) [65] to compute the strength and trajectory of the vortex ring as it propagates towards and interacts with the IPMC. In addition, the obtained images are analyzed to study the transient vibration of the IPMC and explore its correlation with the vortex dynamics. A cross section of the vortex ring, as acquired from PIV, is seen in Fig. 9.10 along with

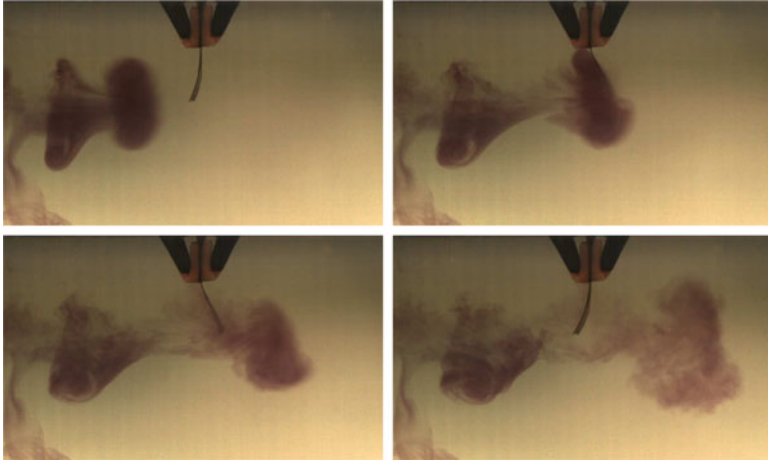


Fig. 9.9 Flow visualization images of a vortex ring impacting a cantilevered strip adapted from [59]

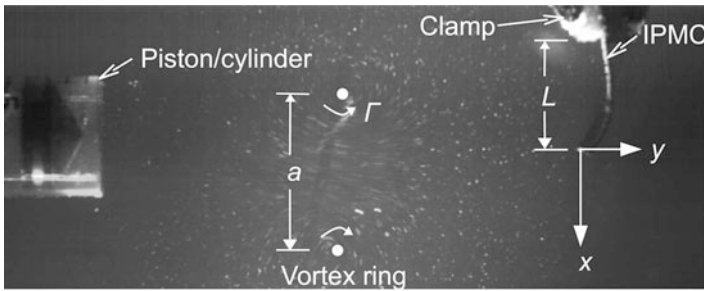


Fig. 9.10 Image of the experimental configuration with overlaid coordinate system and variable definitions (Reprinted with permission from [58]. Copyright 2011, American Institute of Physics)

pertinent nomenclature. The vortex ring circulation is denoted as Γ , its velocity is V_{vr} , and the diameter is termed a .

The circulation of the vortex is estimated by computing the line integral of the velocity field around each of the two vortices appearing in the two-dimensional slice through the center of the ring. Each experiment time is shifted so that t equals zero when the vortex ring is at $y = -2.5 L$. The tip displacement of the IPMC, referred to as δ , is tracked in the sequence of images using a commercial software.

The physics of the interaction can be represented through three primary dimensionless parameters under the following assumptions: the fluid dynamics is modeled using potential flow theory, the vortex ring is assimilated to a vortex pair of equal and opposite circulation, and the beam is described as a Kirchhoff–Love plate undergoing cylindrical bending [59]. The mass ratio $\mu_1 = m/(\rho w L)$ relates the inertia of the beam to the inertia of the fluid and is equal to $\mu_1 = 0.019$. The second

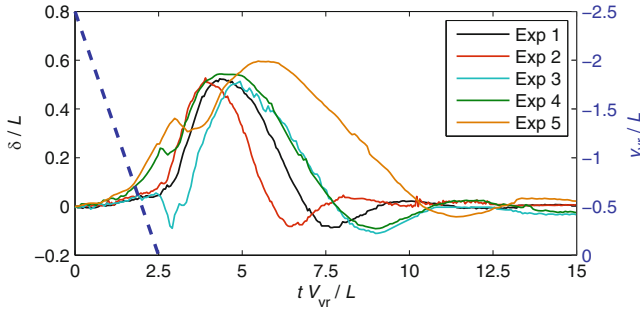


Fig. 9.11 Scaled deflection at the IPMC tip as a function of the nondimensional time tV_{vr}/L for five different experiments along with a curve indicating the vortex ring y -position on the secondary axis (Reprinted with permission from [58]. Copyright 2011, American Institute of Physics)

dimensionless parameter $\mu_2 = B/(\rho\Gamma^2L)$ is the ratio of the restoring force in the IPMC to the fluid loading. The final parameter is a geometric parameter relating the vortex ring length scale a to the IPMC length scale L as $\mu_3 = a/L$.

Figure 9.11 displays the tip deflection as a function of time for five experiments under comparable flow conditions; the experiments are labeled as one through five (Exp 1: $\mu_2 = 0.073$, $\mu_3 = 1.3$, and $V_{vr} = 0.55$ m/s; Exp 2: $\mu_2 = 0.06$, $\mu_3 = 1.3$, and $V_{vr} = 0.46$ m/s; Exp 3: $\mu_2 = 0.03$, $\mu_3 = 1.5$, and $V_{vr} = 0.73$ m/s; Exp 4: $\mu_2 = 0.04$, $\mu_3 = 1.4$, and $V_{vr} = 0.78$ m/s; and Exp 5: $\mu_2 = 0.05$, $\mu_3 = 1.5$, and $V_{vr} = 0.80$ m/s). Included in the plot is the y -position of the vortex ring on the secondary axis y_{vr} . The maximum deflection experienced by the IPMC due to the impact is in the range $0.5 - 0.6L$ and the maximum deflection is reached after the vortex ring breaks down. When the vortex ring reaches the rest position of the IPMC, the deflection is typically not greater than $0.1 - 0.2L$ and only afterwards does the IPMC tip speed increase, suggesting that vortex breakdown plays a critical role in the energy exchange. This phenomenon is indeed not observed in the absence of viscosity, wherein secondary vortical structures are not generated [59]. After the impact takes place, the IPMC vibrates in its fundamental mode shape in a highly damped manner, ultimately returning to rest.

The energy transfer from the fluid to the solid is estimated from the energy associated with the vortex ring core and kinetic energy and the maximum strain energy in the IPMC. The former quantity is computed by using a thin core approximation with hollow core of constant volume [79], which yields 7.6, 5.5, 17.2, 15.6, and 16.8 mJ for experiments one through five, respectively. The maximum strain energy of the IPMC is estimated from the maximum tip deflection by using the fundamental mode of vibration of a cantilever beam, which yields 89, 83, 88, 96, and 120 μ J for experiments one through five, respectively. Therefore, the energy transfer computed as the ratio between the input fluid energy and the elastic energy ranges between 0.5 and 1.5%.

In contrast with the steady flow and the oscillatory experiments, the electrical response from the IPMC in this experiment is purely transient. In this case, the potential for energy harvesting is measured by estimating the electrical energy stored in the IPMC during the interaction in short circuit conditions. Thus, we find that the energy transduced into electrical form is 0.56, 0.62, 0.23, 0.56, and 1.5 nJ for experiments one through five. This indicates that the energy transfer from strain energy into electrical is in line with previously observed conversion rates on the order of 0.0003%–0.0012%.

9.6 Summary and Conclusions

In this chapter, we have presented a few implementations of IPMCs as energy harvesting devices for underwater applications. Specifically, we have described the potential use of such active materials in scavenging energy from steady and oscillatory flows and from coherent fluid structures. In this context, IPMCs offer several advantages over more commonly used active materials, including high compliance, ability of working in wet environments, and good potential for energy storage due to their large electrical capacitance. Another main advantage of these materials is that their electromechanical behavior is largely dictated by surface rather than volumetric properties, which hints at the potential for miniaturization. Nevertheless, the energy conversion rate of this material is currently inferior to more conventional active materials, such as piezoelectrics; yet, we foresee that the current efforts on IPMC fabrication will continue to improve their performance. We also note that the methodologies explored in this book chapter are not strictly confined to IPMCs as the energy harvesters nor to water as the fluid medium. Moreover, the fundamental knowledge developed in the analysis of fluid-structure interactions through direct IPMC-based strain measurement is expected to aid complementary studies on dynamic loading of marine structures.

Acknowledgements This research was supported by the National Science and Engineering Research Council, the National Science Foundation, and the Office of Naval Research under grant numbers 386282-2010, CMMI-0745753 and CMMI-0926791, and N00014-10-1-0988, respectively. The authors would also like to thank the students Matteo Aureli, Emre Basaran, Alberto Giacomello, and Chekema Prince who have contributed to the research efforts summarized in this chapter.

References

1. Abdelnour K, Mancina E, Peterson SD, Porfiri M (2009) Hydrodynamics of underwater propulsors based on ionic polymer metal composites: a numerical study. *Smart Mater Struct* 18(8):085,006
2. Akaydin HD, Elvin N, Andreopoulos Y (2010) Energy harvesting from highly unsteady fluid flows using piezoelectric materials. *J Intell Mater Syst Struct* 21(13):1263–1278

3. Akle BJ, Bennet MD, Leo DJ, Wiles KB, McGrath JE (2007) Direct assembly process: a novel fabrication technique for large strain ionic polymer transducers. *J Mater Sci* 42(16):7031–7041
4. Akle BJ, Leo DJ (2008) Single-walled carbon nanotubes – ionic polymer electroactive hybrid transducers. *J Intell Mater Syst Struct* 19(8):905–915
5. Alben S (2008) The flapping-flag instability as a nonlinear eigenvalue problem. *Phys Fluid* 20:104,106
6. Allen JJ, Smits AJ (2001) Energy harvesting eel. *J Fluid Struct* 15(3–4):629–640
7. Anton S, Sodano H (2007) A review of power harvesting using piezoelectric materials (2003–2006). *Smart Mater Struct* 16(3):R1–R21
8. Aureli M, Basaran ME, Porfiri M (2012) Nonlinear finite amplitude vibrations of sharp-edged beams in viscous fluids. *J Sound Vib* 331(7):1624–1654
9. Aureli M, Kopman V, Porfiri M (2010) Free-locomotion of underwater vehicles actuated by ionic polymer metal composites. *IEEE ASME Trans Mechatron* 15(4):603–614
10. Aureli M, Lin W, Porfiri M (2009) On the capacitance-boost of ionic polymer metal composites due to electroless plating: theory and experiments. *J Appl Phys* 105:104,911
11. Aureli M, Porfiri M (2012) Nonlinear sensing of ionic polymer metal composites. *Continuum Mech Therm*. (DOI 10.1007/s00161-012-0253-x)
12. Aureli M, Porfiri M (2010) Low frequency and large amplitude oscillations of cantilevers in viscous fluids. *Appl Phys Lett* 96(16):164,102
13. Aureli M, Prince C, Porfiri M, Peterson SD (2010) Energy harvesting from base excitation of ionic polymer metal composites in fluid environments. *Smart Mater Struct* 19(1):015,003
14. Bard A, Faulkner L (1980) *Electrochemical methods*. Wiley, New York
15. Bonomo C, Brunetto P, Fortuna L, Giannone P, Graziani S, Strazzeri S (2008) A tactile sensor for biomedical applications based on IPMCs. *IEEE Sensor J* 8(7–8):1486–1493
16. Bonomo C, Fortuna L, Giannone P, Graziani S (2006) A circuit to model the electrical behavior of an ionic polymer-metal composite. *IEEE Trans Circ Syst* 53(2):338–350
17. Bonomo C, Fortuna L, Giannone P, Graziani S, Strazzeri S (2007) A nonlinear model for ionic polymer metal composites as actuators. *Smart Mater Struct* 16(1):1–12
18. Bonomo C, Fortuna L, Giannone P, Graziani S, Strazzeri S (2006) A model for ionic polymer metal composites as sensors. *Smart Mater Struct* 15(3):749–758
19. Bonomo C, Fortuna L, Giannone P, Graziani S, Strazzeri S (2008) A resonant force sensor based on ionic polymer metal composites. *Smart Mater Struct* 17(1):015,014
20. Brufau-Penella J, Puig-Vidal M, Giannone P, Graziani S, Strazzeri S (2008) Characterization of the harvesting capabilities of an ionic polymer metal composite device. *Smart Mater Struct* 17(1):015,009
21. Bryant M, Garcia E (2011) Modeling and testing of a novel aeroelastic flutter energy harvester. *J Vib Acoust* 133(1):011,010
22. Chen Z, Hedgepeth D, Tan X (2009) A nonlinear, control-oriented model for ionic polymer-metal composite actuators. *Smart Mater Struct* 18(5):055,008
23. Chen Z, Tan X, Will A, Ziel C (2007) A dynamic model for ionic polymer-metal composite sensors. *Smart Mater Struct* 16(4):1477–1488
24. Connell B, Yue D (2007) Flapping dynamics of a flag in a uniform stream. *J Fluid Mech* 581:33–67
25. Crighton D, Oswell J (1991) Fluid loading with mean flow. I. Response of an elastic plate to localized excitation. *Phil Trans Phys Sci Eng* 335(1639):557–592
26. Del Bufalo G, Placidi L, Porfiri M (2008) A mixture theory framework for modeling mechanical actuation of ionic polymer metal composites. *Smart Mater Struct* 17(4):045,010
27. Deole U, Lumia R, Shahinpoor M, Bermudez M (2008) Design and test of IPMC artificial muscle microgripper. *J Micro Nano Mechatron* 4(3):1865–3936
28. Erturk A, Inman DJ (2008) A distributed parameter electromechanical model for cantilevered piezoelectric energy harvesters. *Trans ASME J Vib Acoust* 130(4):041,002
29. Erturk A, Inman DJ (2009) An experimentally validated bimorph cantilever model for piezoelectric energy harvesting from base excitations. *Smart Mater Struct* 18(2):025,009
30. Erturk A, Inman DJ (2011) *Piezoelectric energy harvesting*. Wiley, Chichester, West Sussex

31. Erturk A, Vieira WGR, De Marqui Jr, C, Inman DJ (2010) On the energy harvesting potential of piezoaeroelastic systems. *Appl Phys Lett* 96(18):184,103
32. Falcucci G, Aureli M, Ubertini S, Porfiri M (2011) Transverse harmonic oscillations of laminae in viscous fluids: a lattice boltzmann study. *Phil Trans Roy Soc A Math Phys Eng Sci* 369(1945):2456–2466
33. Fang BK, Ju MS, Lin CCK (2007) A new approach to develop ionic polymer-metal composites (IPMC) actuator: Fabrication and control for active catheter systems. *Sensor Actuator A Phys* 137(2):321–329
34. Farinholt K, Leo DJ (2004) Modelling of electromechanical charge sensing in ionic polymer transducers. *Mech Mater* 36(5):421–433
35. Farinholt K, Pedrazas N, Schluneker D, Burt D, Farrar C (2009) An energy harvesting comparison of piezoelectric and ionically conductive polymers. *J Intell Mater Syst Struct* 20(5):633–642
36. Giacomello A, Porfiri M (2011) Underwater energy harvesting from a heavy flag hosting ionic polymer metal composites. *J Appl Phys* 109(8):084,903
37. Gutta S, Lee JS, Trabia MB, Yim W (2009) Modeling of ionic polymer metal composite actuator dynamics using a large deflection beam model. *Smart Mater Struct* 18(11):115,023
38. Guyomar D, Badel A, Lefeuvre E, Richard C (2005) Toward energy harvesting using active materials and conversion improvement by nonlinear processing. *IEEE Trans Ultrason Ferroelectrics Freq Contr* 52(4):584–595
39. Guyomar D, Sebald G, Lefeuvre E, Khodayari A (2009) Toward heat energy harvesting using pyroelectric material. *J Intell Mater Syst Struct* 20(3):265–271
40. Inman D, Grisso B (2006) Towards autonomous sensing. In: Tomizuka M, Yun CB, Giurgiutiu V (eds) *Proc. SPIE smart structures and materials 2006: sensors and smart structures technologies for civil, mechanical, and aerospace systems*, vol. 6174. San Diego, CA, USA, pp. 61,740T:1–7
41. Jo C, Naguib HE, Kwon RH (2008) Modeling and optimization of the electromechanical behavior of an ionic polymer-metal composite. *Smart Mater Struct* 17(6):065,022
42. Kamamichi N, Yamakita M, Asaka K, Luo ZW (2006) A snake-like swimming robot using IPMC actuator/sensor. In: *Proc. 2006 IEEE international conference on robotics and automation*, pp. 1812–1817
43. Kauffman J, Lesieutre G (2009) A low-order model for the design of piezoelectric energy harvesting devices. *J Intell Mater Syst Struct* 20(5):495–504
44. Kim K, Shahinpoor M (2003) Ionic polymer-metal composites: II. Manufacturing techniques. *Smart Mater Struct* 12(1):65–79
45. Kruusmaa M, Hunt A, Punning A, Anton M, Aabloo A (2008) A linked manipulator with ion-polymer metal composite (IPMC) joints for soft- and micromanipulation. In: *Proc. 2008 IEEE international conference on robotics and automation*, pp. 3588–3593
46. Lefeuvre E, Badel A, Richard C, Guyomar D (2007) Energy harvesting using piezoelectric materials: case of random vibrations. *J Electroceramics* 19(4):349–355
47. Leonov V, Torfs T, Fiorini P, Van Hoof C (2007) Thermoelectric converters of human warmth for self-powered wireless sensor nodes. *IEEE Sensor J* 7(5):650–657
48. Mansfield EH (1989) *The bending and stretching of plates*, 2nd edn. Cambridge University Press, New York
49. Mateu L, Moll F (2005) Review of energy harvesting techniques and applications for microelectronics. In: Lopez JF, Fernandez FV, Lopez-Villegas JM, de la Rosa JM (eds) *Proc. SPIE VLSI circuits and systems II*, vol. 5837. Sevilla, Spain, pp. 359–373
50. Mbemmo E, Chen Z, Shatara S, Tan X (2008) Modeling of biomimetic robotic fish propelled by an ionic polymer-metal composite actuator. In: *Proc. 2008 IEEE international conference on robotics and automation*, pp. 689–694
51. Mitcheson P, Yeatman E, Rao G, Holmes A, Green T (2008) Energy harvesting from human and machine motion for wireless electronic devices. *Proc IEEE* 96(9):1457–1486
52. Murray R, Rastegar J (2009) Novel two-stage piezoelectric-based ocean wave energy harvesters for moored or unmoored buoys. In: Ahmadian M, Ghasemi-Nejhad MN (eds) *Proc.*

- SPIE active and passive smart structures and integrated systems 2009, vol. 7288. San Diego, CA, USA, p. 72880E
53. Myers R, Vickers M, Kim H, Priya S (2007) Small scale windmill. *Appl Phys Lett* 90(5):054,106
 54. Nemat-Nasser S (2002) Micromechanics of actuation of ionic polymer-metal composites. *J Appl Phys* 92(5):2899–2915
 55. Nemat-Nasser S, Li J (2000) Electromechanical response of ionic polymer-metal composites. *J Appl Phys* 87(7):3321–3331
 56. Nemat-Nasser S, Thomas C (2004) Ionomeric polymer-metal composites electroactive polymer (EAP) Actuators as artificial muscles - reality, potential and challenges, Chap. 6. SPIE Press, Bellingham, WA
 57. Newbury K, Leo DJ (2003) Linear electromechanical model of ionic polymer transducers-part I: model development. *J Intell Mater Syst Struct* 14(6):333–342
 58. Peterson SD, Porfiri M (2012) Energy exchange between a vortex ring and an ionic polymer metal composite. *Appl Phys Lett* 100(11):114,102
 59. Peterson SD, Porfiri M (2012) Interaction of a vortex pair with a flexible plate in an ideal quiescent fluid. *J Intell Mater Syst Struct* 23(13):1482–1501
 60. Peterson SD, Porfiri M, Rovardi A (2009) A particle image velocimetry study of vibrating ionic polymer metal composites in aqueous environments. *IEEE ASME Trans Mechatron* 14(4):474–483
 61. Porfiri M (2008) Charge dynamics in ionic polymer metal composites. *J Appl Phys* 104(10):104,915
 62. Porfiri M (2009) An electromechanical model for sensing and actuation of ionic polymer metal composites. *Smart Mater Struct* 18(1):015,016
 63. Porfiri M (2009) Influence of electrode surface roughness and steric effects on the nonlinear electromechanical behavior of ionic polymer metal composites. *Phys Rev E* 79(4):041,503
 64. Qin Z, Batra RC (2009) Local slamming impact of sandwich composite hulls. *Int J Solid Struct* 46(10):2011–2035
 65. Raffel M, Willert C, Wereley S, Kompenhans J (2007) Particle image velocimetry: a practical guide. Springer, Berlin
 66. Rastegar J, Pereira C, Nguyen H (2006) Piezoelectric-based power sources for harvesting energy from platforms with low-frequency vibration. In: White EV (ed) *Proc. SPIE Smart Structures and Materials 2006: Industrial and Commercial Applications of Smart Structures Technologies*, vol. 6171. San Diego, CA, USA, pp. 617,101:1–7
 67. Renno J, Daqaq M, Inman D (2009) On the optimal energy harvesting from a vibration source. *J Sound Vib* 320(1–2):386–405
 68. Roundy S (2005) On the effectiveness of vibration-based energy harvesting. *J Intell Mater Syst Struct* 16(10):809–823
 69. Sader JE (1998) Frequency response of cantilever beams immersed in viscous fluids with applications to the atomic force microscope. *J Appl Phys* 84(1):64–76
 70. Shahinpoor M, Bar-Cohen Y, Simpson JO, Smith J (1998) Ionic polymer-metal composites (IPMCs) as biomimetic sensors, actuators and artificial muscles-a review. *Smart Mater Struct* 7(6):R15–R30
 71. Shahinpoor M, Kim K (2001) Ionic polymer-metal composites: I. Fundamentals. *Smart Mater Struct* 10(4):819–833
 72. Shahinpoor M, Kim K (2004) Ionic polymer-metal composites: III. Modeling and simulation as biomimetic sensors, actuators, transducers, and artificial muscles. *Smart Mater Struct* 13(6):1362–1388
 73. Shahinpoor M, Kim K (2005) Ionic polymer-metal composites: IV. Industrial and medical applications. *Smart Mater Struct* 14(1):197–214
 74. Shelley M, Vandenbergh N, Zhang J (2005) Heavy flags undergo spontaneous oscillations in flowing water. *Phys Rev Lett* 94(9):94,302
 75. Sodano H, Inman D, Park G (2004) A review of power harvesting from vibration using piezoelectric materials. *Shock Vib Digest* 36:197–205

76. Sodano HA, Inman DJ, Park G (2005) Comparison of piezoelectric energy harvesting devices for recharging batteries. *J Intell Mater Syst Struct* 16(10):799–807
77. Sodano HA, Inman DJ, Park G (2005) Generation and storage of electricity from harvesting devices. *J Intell Mater Syst Struct* 16(1):67–75
78. St. Clair D, Bibo A, Sennakesavababu VR, Daqaq MF, Li G (2010) A scalable concept for micro-power generation using flow-induced self-excited oscillations. *Appl Phys Lett* 96(14):144,103
79. Sullivan IS, Niemela JJ, Hershberger RE, Bolster D, Donnelly RJ (2008) Dynamics of thin vortex rings. *J Fluid Mech* 609:319–347
80. Tang L, Païdoussis M (2008) The influence of the wake on the stability of cantilevered flexible plates in axial flow. *J Sound Vib* 310(3):512–526
81. Taylor GW, Burns JR, Kammann SM, Powers WB, Welsh TR (2001) The energy harvesting eel: A small subsurface ocean/river power generator. *IEEE J Ocean Eng* 26(4):539–547
82. Tiwari R, Kim K, Kim S (2008) Ionic polymer-metal composite as energy harvesters. *Smart Struct Syst* 4(5):549–563
83. Tuck EO (1969) Calculation of unsteady flows due to unsteady motion of cylinders in a viscous fluid. *J Eng Math* 3(1):29–44
84. Wallmersperger T, Akle B, Leo D, Kroplin B (2008) Electrochemical response in ionic polymer transducers: an experimental and theoretical study. *Compos Sci Tech* 68(5):1173–1180
85. Wallmersperger T, Kroplin B, Gulch R (2004) Coupled chemo-electro-mechanical formulation for ionic polymer gels-numerical and experimental investigations. *Mech Mater* 36(5–6): 411–420
86. Wallmersperger T, Leo DJ, Kothera CS (2007) Transport modeling in ionomeric polymer transducers and its relationship to electromechanical coupling. *J Appl Phys* 101(2):024,912
87. Yeatman E (2009) Energy harvesting: small scale energy production from ambient sources. In: Ahmadian M, Ghasemi-Nejhad MN (eds) *Proc. SPIE Active and Passive Smart Structures and Integrated Systems 2009*, vol. 7288. San Diego, CA, USA, p. 728802
88. Yeom SW, Oh IK (2009) A biomimetic jellyfish robot based on ionic polymer metal composite actuators. *Smart Mater Struct* 18(8):085,002